

# The transition from brittle faulting to cataclastic flow: Permeability evolution

Wenlu Zhu and Teng-fong Wong

Department of Earth and Space Sciences, State University of New York at Stony Brook

**Abstract.** Triaxial compression experiments were conducted to investigate influences of stress and failure mode on axial permeability of five sandstones with porosities ranging from 15% to 35%. In the cataclastic flow regime, permeability and porosity changes closely track one another. A drastic decrease in permeability was triggered by the onset of shear-enhanced compaction caused by grain crushing and pore collapse. The compactive yield stress  $C^*$  maps out a boundary in stress space separating two different types of permeability evolution. Before  $C^*$  is attained, permeability and porosity both decrease with increasing effective mean stress, but they are independent of deviatoric stresses. However, with loading beyond  $C^*$ , both permeability and porosity changes are strongly dependent on the deviatoric and effective mean stresses. In the brittle faulting regime, permeability and porosity changes are more complex. Before the onset of shear-induced dilation  $C'$ , both permeability and porosity decrease with increasing effective mean stress. Beyond  $C'$ , permeability may actually decrease in a dilating rock prior to brittle failure. After the peak stress has been attained, the development of a relatively impermeable shear band causes an accelerated decrease of permeability. Permeability evolution in porous sandstones is compared with that in low-porosity crystalline rocks. A conceptual model for the coupling of deformation and fluid transport is proposed in the form of a deformation-permeability map.

## Introduction

Fluid exerts significant mechanical and chemical effects on crustal processes, with important consequences in seismotectonics, economic geology, petroleum geology, aqueous geochemistry, and geotechnical engineering [Bredenhoeft and Norton, 1990; Torgersen, 1991]. Fluid transport in porous media is generally governed by Darcy's law. To model the fluid percolation process in a specific lithological and tectonic setting, one of the most difficult problems has been the estimation of permeability. A wide range of pressure, temperature, and stress state are encountered in natural tectonic, metamorphic, and diagenetic processes. Laboratory measurements of permeability under crustal conditions of pressure, temperature, and stress can therefore provide important insight into the coupling of deformation and fluid transport. Although preliminary attempts have been made by, for example, Fischer and Paterson [1992] to conduct permeability measurements under elevated temperatures and nonhydrostatic loading, most experimental data on the effect of stress on permeability have been obtained under room temperature conditions.

For low-porosity rocks, such laboratory studies have provided a fairly complete picture of how permeability depends on porosity and deformation mechanism. In a low-porosity rock, dilatancy is generally observed whether the rock fails by brittle faulting or cataclastic flow. Microstructural observations have shown that dilation of the pore space is primarily induced by pervasive stress-induced microcracking, which increases the permeability by widening the apertures and enhancing the connectivity of the flow paths. In the brittle faulting regime,

Zoback and Byerlee [1975] observed that permeability increased by a factor of  $\sim 3$  as a sample of Westerly granite was stressed to  $\sim 80\%$  of the peak stress. In the cataclastic flow regime, recent measurements on halite [Peach and Spiers, 1996; Stormont and Daemen, 1992], Carrara marble, and hot-pressed calcite [Zhang *et al.*, 1994] show even more pronounced enhancement of the permeability (by several orders of magnitude) with the accumulation of strain (of several percent).

In contrast, the current understanding of the effect of stress on permeability in porous rocks (with porosity  $> 5\%$  or so) is less comprehensive. In an insightful review, Brace [1978a] underscored some of the key problems that are still not completely resolved. Does permeability increase or decrease with deformation? In the brittle regime, apparently contradictory observations in sandstones were reported. Whereas Mordecai and Morris [1971] measured an increase of  $\sim 20\%$  in permeability prior to brittle faulting in Darley Dale sandstone, Gatto [1984] observed that permeability consistently decreased with increasing stress in Berea sandstone. In the cataclastic flow regime, the application of nonhydrostatic stresses usually causes the pore space in a high-porosity rock to compact and permeability to decrease. How does permeability evolve as a function of the stress state? Somerton *et al.* [1975] concluded that in coal, permeability was primarily dependent on the mean stress and nonhydrostatic stress had negligible influence. On the other hand, Nelson [1981], Holt [1989], and Rhett and Teufel [1992] observed that permeability evolution in sandstone was very sensitive to loading path through the interplay of hydrostatic and nonhydrostatic loadings.

With these questions in mind we investigated the permeability as a function of stress states spanning the brittle-ductile transition in the Adamswiller, Berea, Boise, Darley Dale, and Rothbach sandstones. The nominal porosities of these sandstones range from 15% to 35%, and the mechanical behavior and failure mode in relation to the transition from brittle faulting to compactive

Copyright 1997 by the American Geophysical Union.

Paper number 96JB03282  
0148-0277/97/96JB-03282\$09.00

cataclastic flow have been investigated in some detail [Wong *et al.*, this issue]. The two deformation regimes are associated with distinct patterns of porosity change, acoustic emission, and microcracking activities. The correlation of permeability with the mechanical deformation and failure mode will be investigated.

### Experimental Procedure

Petrophysical description of the sandstones (including porosity, grain size, and modal analysis) was provided by Wong *et al.* [this issue]. The Berea, Boise, Darley Dale, and Rothbach sandstone samples were cored perpendicular to bedding, whereas the Adamswiller sandstone samples were cored parallel to the bedding. All the samples were ground to a cylindrical shape, with diameter of 18.4 mm and length 38.1 mm (except the Darley Dale sandstone samples that had diameters of 19.9 mm and lengths of 40.6 mm). Before each test the sample was vacuum saturated with distilled water, jacketed with copper foil, and positioned between two steel end-plugs, each of which has a concentric hole at the center for fluid access to the upstream or downstream pore pressure system. Heat-shrink polyolefine tubing was used to separate the sample from the confining pressure medium (kerosene).

The samples were then deformed at room temperature in the conventional triaxial configuration, with the axial stress  $\sigma_1 > \sigma_2 = \sigma_3$ . The confining pressures  $P_c (= \sigma_3)$  were fixed at values in the range from 13 to 550 MPa, while the pore pressure  $P_p$  was fixed at 10 MPa. After the specific confining and pore pressures had been attained, the differential stress was applied by a servo-controlled hydraulic system. The nominal strain rate of  $5 \times 10^{-3}/s$  was sufficiently slow to ensure a fully "drained" condition. Technical details on the mechanical deformation measurements

were provided by Wong *et al.* [this issue]. At different stages of deformation the loading ram was locked and the in situ permeability was measured for hydraulic flow in the axial ( $\sigma_1$ ) direction. In each test the initial permeability was measured at  $P_c = 13$  MPa and  $P_p = 10$  MPa (corresponding to an effective pressure of  $P_c - P_p = 3$  MPa) to prevent leakage along the sample-jacket interface.

In a typical test the permeability  $k$  would change by 3 to 5 orders of magnitude. We have modified Bernabé's [1987] design of a wide-range permeameter (originally for hydrostatic loading) for operation in a triaxial system. Two different techniques can be implemented, depending on the permeability of interest. If the permeability at a certain stress state is relatively high ( $k > 10^{-16}$  m<sup>2</sup>), it is measured by the steady-state flow technique. For  $k < 10^{-16}$  m<sup>2</sup>, thermal fluctuation would render it difficult to achieve steady state flow, and instead we use the pulse transient technique of Brace *et al.* [1968]. A schematic diagram of the wide-range permeameter is shown in Figure 1. The accumulator and volumometer play important roles in the permeability and deformation measurements, respectively. During loading the accumulator was disconnected from the system (by closing valve 2) and the volumometer was used to monitor the pore volume change. Corresponding adjustment of the fluid storage in the volumometer was made to maintain the pore pressure at the constant value of 10 MPa.

When loading was stopped and the ram locked, the accumulator was connected (by opening valve 2) to maintain a constant pore pressure during the permeability measurements. For relatively permeable samples, valve 4 was closed to isolate the accumulator and volumometer from the downstream. While the accumulator maintained the upstream pore pressure constant at  $P_p = 10$  MPa, the meter valve was opened by a small amount

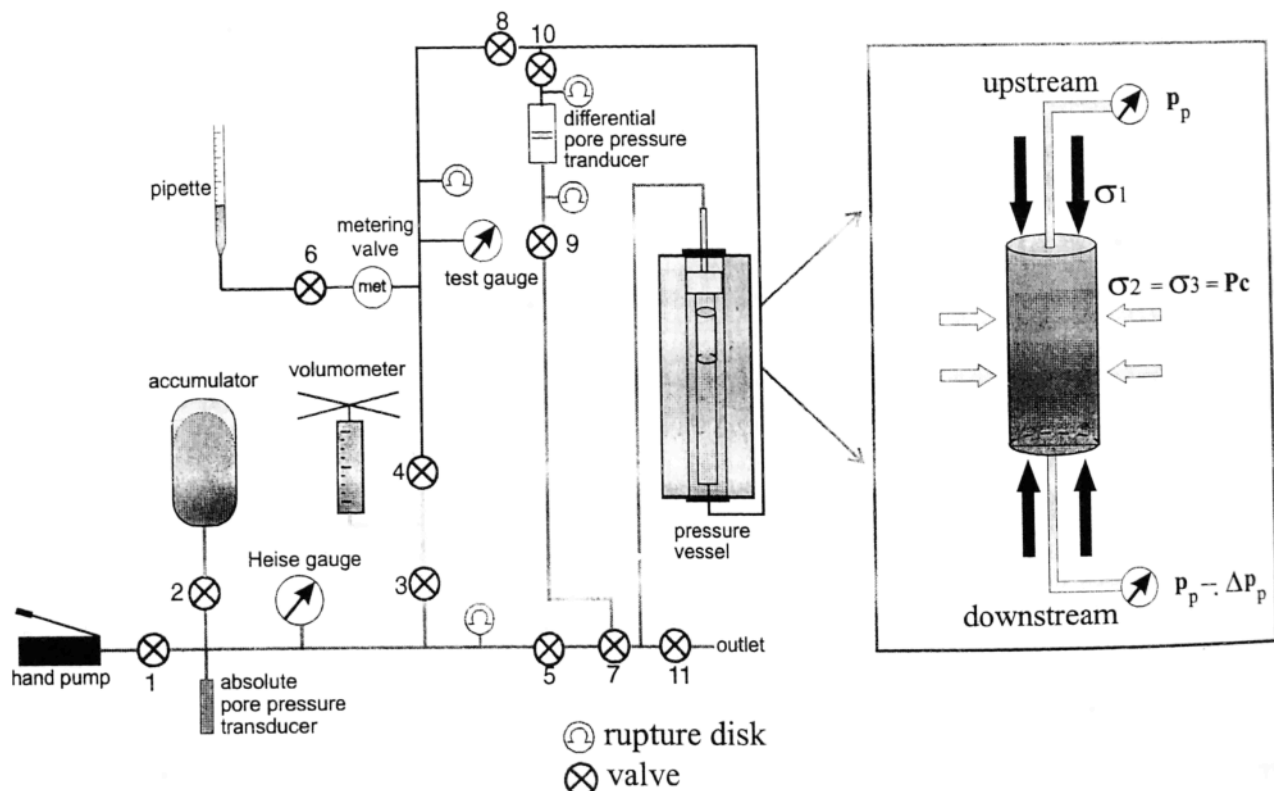


**Figure 1.** Schematic diagram of a wide-range permeameter. The steady state flow or pulse transient technique can be used on a sample loaded in the conventional triaxial configuration (modified from Bernabé's [1987] technique).

to decrease the downstream pressure by a constant increment of  $\Delta P_p$ , inducing the fluid from upstream to percolate in steady state through the sample. For relatively impermeable samples, valve 6 was closed to inhibit drainage from the downstream system. valve 3 (instead of valve 4) was also closed to isolate the accumulator and connect the volumeter to the downstream. The volumeter piston was displaced instantaneously by a small increment, inducing a pore pressure pulse of magnitude  $\Delta P_p$  in the downstream reservoir. The difference in pore pressures between upstream and downstream induces a transient flow through the sample, manifested by a temporal decay of the differential pressure across the sample. Hsieh *et al.* [1981] have derived the exact solution for the pressure transient, which is sensitively dependent on the storage characteristics. In our setup, the compressive storage of the upstream reservoir is  $3.18 \times 10^{-8}$  m<sup>3</sup>/MPa and that of downstream is effectively infinite due to the significant storage of the accumulator. These values fall within the parameter space in which the transient can be approximated as an exponential decay [Neuzil *et al.* 1981; Bernabé, 1987]. Accordingly, the permeability can be inferred from the slope of a semilog plot of the differential pressure transducer data versus time, following the procedure pioneered by Brace *et al.* [1968].

The transducer can resolve pressure difference down to 20 kPa, which is the major factor limiting the accuracy in our permeability measurement. For most of the our tests, the uncertainty of the permeability measurements is < 15%. The reproducibility of our measurements was also within 15%. In the present configuration, the permeameter is limited to samples with  $k < 0.2 \times 10^{-12}$  m<sup>2</sup> above which a pressure difference ( $\Delta P_p < 20$  kPa) too small to be resolved is required to obtain a sufficiently slow flow rate.

## Experimental Results

For reference we have compiled in Table 1 the axial permeability data versus effective pressure and porosity for hydrostatic loading. All the triaxial compression data for permeability versus stress, axial strain, and porosity are compiled in Table 2. Since the mechanical and transport properties of Berea sandstone have been studied most thoroughly, we will first describe in some detail its permeability evolution before moving on to the other four sandstones. The differential stress and permeability as functions of the axial strain for triaxial experiments at effective pressures of 5, 10, 40, 160, and 250 MPa are shown in Figure 2. The permeability and porosity as functions of the effective mean stress  $((\sigma_1 + 2\sigma_3)/3 - P_p)$  for samples which failed by compactive cataclastic flow and by shear localization are shown in Figures 3a and 3b, respectively. The permeability as a function of porosity for the cataclastic flow and brittle faulting regimes are shown in Figures 4a and 4b, respectively. For reference, the permeability evolution under hydrostatic loading (from Table 1) are included in Figures 3 and 4 as dashed curves. Effective pressure by itself reduced the permeability of Berea sandstone by about 3 orders of magnitude, with the most significant drop occurring after the onset of grain crushing at the critical effective pressure  $P^*$  [David *et al.*, 1994].

The stress-strain curves in Figure 2 are similar to those of samples that were subjected to continuous loading at corresponding effective pressures [Wong *et al.*, this issue]. However, there is a minor difference in that the differential stress level for the corresponding axial strain was somewhat lower in the former case, possibly due to stress corrosion processes operative during the "hold" phases when permeability measurements were conducted. The most important feature of

Table 1. Hydrostatic Tests

Effective Pressure ( $P_c - P_p$ ), MPa	Porosity $\phi$ , %	Permeability $k$ , $\times 10^{-15}$ m <sup>2</sup>
<i>Adamswiller</i>		
3.0	23.00	144.20
10.0	22.01	52.20
20.0	21.36	21.05
40.0	21.00	10.01
70.0	20.55	5.48
110.0	20.01	3.68
150.0	19.49	2.44
190.0	18.82	2.22
230.0	16.96	1.22
250.0	15.97	0.73
300.0	13.07	0.17
365.0	10.40	0.15
<i>Berea</i>		
3.0	21.00	348.40
5.0	20.76	223.10
10.0	20.26	160.40
20.0	19.83	131.60
30.0	19.54	120.30
40.0	19.33	107.30
60.0	18.96	99.30
80.0	18.70	88.80
105.0	18.42	66.20
140.0	18.11	52.40
170.0	17.81	39.10
200.0	17.50	35.10
230.0	17.19	20.30
260.0	16.88	15.80
290.0	16.46	9.10
320.0	16.11	3.44
350.0	15.73	2.33
371.0	14.37	1.00
380.0	13.72	0.75
390.0	13.56	0.69
420.0	13.14	0.52
460.0	12.45	0.38
500.0	11.91	0.29
540.0	11.32	0.21
<i>Boise</i>		
3.0	35.00	1863.80
5.0	34.50	1720.60
10.0	33.48	1650.40
15.0	32.85	1453.40
20.0	32.29	1125.70
25.0	31.95	938.30
30.0	31.27	619.00
35.0	30.55	281.10
40.0	29.74	182.90
45.0	28.97	94.60
50.0	28.28	62.50
55.0	27.90	53.90
60.0	27.40	42.70
70.0	26.51	13.10
80.0	25.97	8.20
90.0	25.50	5.90
100.0	25.01	4.10
110.0	24.60	3.40
120.0	24.20	2.75
140.0	23.57	1.73
160.0	23.04	1.13
180.0	22.55	0.87
200.0	22.10	0.68
220.0	21.69	0.54
240.0	21.28	0.43
<i>Darley Dale</i>		
3.0	14.00	64.50
5.0	13.83	33.90
10.0	13.51	21.60

Table 1. (continued)

Effective Pressure ( $P_c - P_p$ ), MPa	Porosity $\phi$ , %	Permeability $k$ , $\times 10^{-15} \text{ m}^2$
<i>Darley Dale (continued)</i>		
15.0	13.26	15.20
20.0	13.10	11.70
30.0	12.85	8.37
40.0	12.66	7.01
50.0	12.51	5.64
60.0	12.37	4.28
70.0	12.27	3.82
90.0	12.07	2.78
110.0	11.91	2.60
140.0	11.64	2.04
170.0	11.39	1.78
200.0	11.17	1.64
230.0	10.93	1.56
260.0	10.80	1.42
310.0	10.45	0.97
380.0	10.10	0.51
440.0	9.66	0.23
490.0	9.18	0.15
530.0	8.87	0.12
<i>Rothbach</i>		
5.0	19.85	407.90
10.0	19.04	235.20
20.0	17.95	56.70
40.0	17.30	27.60
65.0	16.60	16.80
90.0	16.31	8.96
112.0	15.96	6.90
165.0	15.08	3.20
200.0	14.54	1.52
220.0	14.28	0.90
230.0	14.12	0.51
250.0	13.68	0.27
280.0	12.48	0.11
310.0	11.49	0.07
350.0	10.16	0.04
390.0	9.52	0.03

Table 2. Triaxial Tests

Effective Pressure ( $P_c - P_p$ ), MPa	Differential Stress ( $\sigma_1 - \sigma_3$ ), MPa	Porosity $\phi$ , %	Axial Strain $\epsilon$ , %	Permeability $k$ , $\times 10^{-15} \text{ m}^2$
<i>Adamswiller</i>				
3.0	0.0	23.00		39.80
5.0	0.0	22.65	0.00	22.90
5.0	40.1	21.99	1.00	7.70
5.0	59.1	21.99	1.27	5.30
5.0	73.6	22.22	1.67	3.30
5.0	65.9	22.59	2.31	2.00
5.0	48.5	23.24	3.24	1.92
5.0	46.4	23.41	4.41	1.85
3.0	0.0	23.00		27.90
40.0	0.0	21.86	0.00	9.47
40.0	55.2	21.41	0.45	3.29
40.0	101.4	20.93	1.20	1.45
40.0	109.8	20.72	1.80	0.93
40.0	104.7	20.48	2.60	0.83
40.0	103.5	19.49	3.80	0.67
40.0	103.5	18.68	5.30	0.55
40.0	106.5	17.74	8.30	0.43
40.0	112.8	17.18	12.00	0.31
3.0	0.0	23.00		54.03
10.0	0.0	22.34		26.30

Table 2. (continued)

Effective Pressure ( $P_c - P_p$ ), MPa	Differential Stress ( $\sigma_1 - \sigma_3$ ), MPa	Porosity $\phi$ , %	Axial Strain $\epsilon$ , %	Permeability $k$ , $\times 10^{-15} \text{ m}^2$
40.0	0.0	21.26		6.97
70.0	0.0	20.78		4.95
110.0	0.0	20.31		3.60
150.0	0.0	19.82	0.00	2.75
150.0	57.0	19.22	0.70	1.89
150.0	96.0	18.53	1.30	1.40
150.0	114.0	16.46	3.30	0.66
150.0	159.0	13.02	7.10	0.27
150.0	219.0	10.30	11.50	0.12
150.0	297.0	8.61	17.20	0.07
<i>Berea</i>				
3.0	0.0	21.00		230.70
5.0	0.0	20.44	0.00	207.40
5.0	30.3	19.58	0.80	144.60
5.0	77.3	19.43	1.34	124.20
5.0	80.5	19.94	1.68	96.80
5.0	35.1	20.48	2.12	72.00
5.0	33.0	20.52	2.78	56.40
5.0	36.5	20.51	3.81	50.70
3.0	0.0	21.00		342.80
5.0	0.0	20.42		323.50
10.0	0.0	19.85	0.00	187.50
10.0	77.4	18.91	1.03	135.90
10.0	101.9	19.08	1.57	106.00
10.0	56.8	19.64	2.96	87.20
10.0	60.6	19.77	4.89	69.90
10.0	60.4	19.83	6.89	56.30
3.0	0.0	21.00		579.70
5.0	0.0	20.50		405.00
10.0	0.0	19.63		252.80
20.0	0.0	19.15		195.20
30.0	0.0	18.88		179.00
40.0	0.0	18.68	0.00	164.00
40.0	81.4	18.31	0.63	125.80
40.0	172.2	17.92	1.77	47.60
40.0	163.0	17.81	3.12	17.60
40.0	148.8	17.60	4.55	6.50
40.0	140.0	17.20	6.86	3.20
3.0	0.0	21.00		393.60
5.0	0.0	20.72		310.00
10.0	0.0	20.10		214.60
20.0	0.0	19.45		146.50
30.0	0.0	19.19		129.10
40.0	0.0	18.99		117.80
60.0	0.0	18.64		100.70
80.0	0.0	18.40		94.80
100.0	0.0	18.20		84.50
120.0	0.0	18.01		73.60
140.0	0.0	17.83		69.50
160.0	0.0	17.63	0.00	61.90
160.0	84.9	17.33	0.53	45.30
160.0	180.5	16.93	1.27	36.80
160.0	245.7	16.49	2.04	9.50
160.0	250.8	15.81	3.23	1.56
160.0	247.6	14.86	4.80	1.07
160.0	263.8	13.54	7.16	0.81
3.0	0.0	21.00		456.30
5.0	0.0	20.53		322.50
10.0	0.0	19.87		200.80
20.0	0.0	19.34		166.70
30.0	0.0	19.16		152.40
40.0	0.0	18.96		130.40
60.0	0.0	18.68		110.80
80.0	0.0	18.40		78.60
110.0	0.0	18.06		49.20
140.0	0.0	17.73		30.20

Table 2. (continued)

Effective Pressure ( $P_c - P_p$ ), MPa	Differential Stress ( $\sigma_1 - \sigma_3$ ), MPa	Porosity $\phi$ , %	Axial Strain $\epsilon$ , %	Permeability $k$ , $\times 10^{-15} \text{ m}^2$
<i>Berea (continued)</i>				
170.0	0.0	17.49		25.50
200.0	0.0	17.25		24.70
250.0	0.0	16.71	0.00	22.90
250.0	135.0	16.19	0.79	11.00
250.0	205.6	15.65	1.67	2.00
250.0	203.3	14.88	2.79	1.04
250.0	219.4	14.05	4.04	0.82
250.0	239.7	13.30	5.30	0.49
250.0	278.9	12.37	6.98	0.36
<i>Boise</i>				
3.0	0.0	35.00		2090.50
5.0	0.0	34.39	0.00	1766.00
5.0	15.2	33.43	0.86	1509.20
5.0	26.9	32.74	1.57	1251.00
5.0	25.9	32.22	2.45	854.10
5.0	27.5	31.72	3.42	623.20
5.0	27.9	31.21	4.49	472.60
5.0	26.6	30.66	5.69	412.30
5.0	27.2	29.89	7.70	283.90
3.0	0.0	35.00		2005.60
5.0	0.0	34.21		1560.20
10.0	0.0	33.11		1359.40
15.0	0.0	32.29		1240.30
20.0	0.0	31.68	0.00	1078.50
20.0	18.8	31.05	0.67	674.10
20.0	25.5	30.08	1.66	426.90
20.0	29.3	29.05	2.79	269.90
20.0	32.2	27.85	4.13	206.60
20.0	34.3	26.82	5.42	141.30
20.0	39.7	25.39	7.37	109.80
3.0	0.0	35.00		1553.30
5.0	0.0	34.37		1350.40
10.0	0.0	33.31		1223.80
15.0	0.0	32.56		1154.20
20.0	0.0	32.01		1022.30
25.0	0.0	31.51		876.20
30.0	0.0	31.18	0.00	837.40
30.0	23.8	30.38	0.92	664.70
30.0	31.5	29.45	1.94	422.30
30.0	36.8	28.21	3.30	369.40
30.0	43.3	26.73	4.96	216.30
30.0	46.8	25.82	6.14	140.90
30.0	52.8	24.57	7.73	92.80
<i>Darley Dale</i>				
3.0	0.0	14.50		115.70
5.0	0.0	14.29	0.00	89.00
5.0	29.4	13.90	0.65	40.10
5.0	48.7	13.87	1.00	25.70
5.0	64.1	14.21	1.14	28.80
5.0	57.7	14.97	1.76	25.00
5.0	32.5	15.48	2.36	23.00
5.0	28.9	15.52	3.09	21.50
5.0	30.2	15.57	4.26	19.40
3.0	0.0	14.30		95.70
6.0	0.0	14.03		59.60
10.0	0.0	13.72	0.00	35.60
10.0	68.0	13.28	1.04	13.40
10.0	79.2	13.60	1.52	15.00
10.0	62.5	14.47	2.21	12.00
10.0	45.4	14.74	3.28	10.80
10.0	48.0	14.86	4.65	8.87
10.0	43.9	14.91	6.22	7.36

Table 2. (continued)

Effective Pressure ( $P_c - P_p$ ), MPa	Differential Stress ( $\sigma_1 - \sigma_3$ ), MPa	Porosity $\phi$ , %	Axial Strain $\epsilon$ , %	Permeability $k$ , $\times 10^{-15} \text{ m}^2$
3.0	0.0	14.50		181.90
5.0	0.0	14.27		147.60
10.0	0.0	13.77		84.20
15.0	0.0	13.40		46.10
20.0	0.0	13.16	0.00	35.80
20.0	38.0	12.83	0.44	25.80
20.0	98.0	12.61	1.00	16.30
20.0	120.1	12.77	1.66	12.60
20.0	115.8	13.05	2.21	10.30
20.0	105.8	13.39	3.03	8.64
20.0	96.8	13.58	3.96	7.46
20.0	93.7	13.64	4.71	7.10
3.0	0.0	14.10		101.80
5.0	0.0	13.84		62.60
10.0	0.0	13.39		39.90
15.0	0.0	13.14		30.20
20.0	0.0	12.94		26.10
30.0	0.0	12.72		20.30
40.0	0.0	12.56		14.50
50.0	0.0	12.43		10.60
60.0	0.0	12.33		8.09
80.0	0.0	12.06		4.78
100.0	0.0	11.85	0.00	3.07
100.0	69.4	11.59	0.73	2.36
100.0	132.2	11.30	1.52	1.74
100.0	185.8	10.97	2.50	0.95
100.0	203.3	10.75	3.50	0.47
100.0	215.6	10.39	5.15	0.27
100.0	224.6	10.16	6.96	0.19
3.0	0.0	14.50		190.10
50.0	0.0	14.36		135.00
10.0	0.0	14.13		92.30
20.0	0.0	13.68		65.80
40.0	0.0	13.32		27.60
60.0	0.0	13.04		13.80
90.0	0.0	12.65		7.62
120.0	0.0	12.38		5.06
150.0	0.0	12.15		3.48
180.0	0.0	11.91		2.69
200.0	0.0	11.77	0.00	2.45
200.0	80.0	11.59	0.48	1.50
200.0	143.9	11.36	1.06	1.01
200.0	214.1	11.07	1.86	0.59
200.0	280.8	10.70	3.06	0.27
200.0	303.5	10.52	3.83	0.18
200.0	334.9	10.19	5.07	0.10
200.0	369.3	9.86	6.69	0.06
<i>Rothbach</i>				
3.0	0.0	20.00		129.70
5.0	0.0	19.79	0.00	87.70
5.0	43.4	19.20	0.93	48.60
5.0	63.3	19.36	1.53	26.30
5.0	62.8	20.00	2.02	20.40
5.0	48.3	20.59	2.84	18.60
5.0	37.3	20.93	3.70	17.00
5.0	36.8	21.08	4.70	13.10
5.0	37.2	21.24	5.52	11.60
3.0	0.0	20.00		256.70
10.0	0.0	18.58		65.80
20.0	0.0	18.09	0.00	49.10
20.0	60.0	17.40	1.17	27.90
20.0	80.1	17.06	2.76	23.70
20.0	72.0	16.97	3.69	21.00
20.0	69.9	16.82	6.24	13.90

Table 2. (continued)

Effective Pressure ( $P_c - P_p$ ), MPa	Differential Stress ( $\sigma_1 - \sigma_3$ ), MPa	Porosity $\phi$ , %	Axial Strain $\epsilon$ , %	Permeability $k$ , $\times 10^{-15} \text{ m}^2$
<i>Rothbach (continued)</i>				
3.0	0.0	20.00		93.30
10.0	0.0	19.65		58.40
20.0	0.0	19.24		47.80
65.0	0.0	18.11		32.20
90.0	0.0	17.67		23.50
140.0	0.0	16.93		14.30
165.0	0.0	16.52	0.00	10.20
165.0	66.0	16.37	0.61	5.50
165.0	117.0	16.06	1.75	3.60
165.0	174.0	13.21	6.10	0.28
165.0	249.0	10.24	12.47	0.06
165.0	333.0	8.86	19.70	0.04

our data is that permeability consistently decreases with increasing strain, independent of whether the sample showed strain softening or hardening and whether it failed by shear localization or cataclastic flow. Indeed, the same conclusion holds for all our sandstones (Figure 5), with the exception of the (least porous) Darley Dale sandstone, which showed slight increases of permeability by 12.1% and 11.8% prior to brittle fracture at effective pressures of 5 and 10 MPa, respectively.

Our mechanical data indicate that the failure mode is intimately related to the porosity change behavior. In the cataclastic flow regime, the compaction behavior has the important feature that application of nonhydrostatic stress induces significant reduction of porosity (corresponding to deviation of the solid curves for triaxial compression from the dashed curve for hydrostatic compression in Figure 3a) if the differential stress is increased beyond a threshold. This critical stress state  $C^*$  corresponds to the onset of "shear-enhanced compaction" [Wong *et al.*, this issue]. It can be seen from Figure 3a that the permeability and porosity evolutions in Berea sandstone are intimately related to each other. The critical stress states  $C^*$  also mark the onset of significant reduction of permeability by deviatoric stresses. Before a sample is loaded up to  $C^*$ , the permeability is primarily controlled by the effective mean stress, independent of the deviatoric stresses. However, as soon as the compactive yield stress level  $C^*$  is reached, the nonhydrostatic loading exerts dominant control over the permeability, reducing it by as much as 2 orders of magnitude during cataclastic flow. Since permeability and porosity changes closely track one another, the systematic characterization of porosity reduction during cataclastic flow would provide important clues to the concomitant evolution of permeability. This conclusion is reinforced by our permeability and porosity change data for the other sandstones (Figure 6). If permeability is plotted as a function of porosity, minor differences can be seen between the triaxial and hydrostatic results, but overall the trends are rather similar with a positive correlation between permeability and porosity in the cataclastic flow regime (Figure 4a and Figures 6e-6h).

The porosity and permeability changes of Berea sandstone samples that failed by shear localization are shown as functions of the effective mean stress in Figure 3b. Under effective pressures of 5 and 10 MPa, the nonhydrostatic stress causes porosity to increase relative to the dotted curve for hydrostatic loading. The stress states at which the triaxial data deviate from

the hydrostat are denoted by  $C^*$ , marking the onset of shear-induced dilation [Wong *et al.*, this issue]. There are qualitative differences in the evolution of permeability and porosity with stress. Near  $C^*$  the nonhydrostatic stress results in a slight increase of permeability relative to hydrostatic loading, but subsequently there is an accelerated decrease near the peak stress level.

If permeability is plotted as a function of porosity, they do not track one another in a systematic manner (Figure 4b). Before the onset of dilatancy, permeability and porosity changes were positively correlated. When the samples were loaded to near the peak stress, permeability and porosity changes were actually negatively correlated. In the postfailure stage, shear localization developed and permeability decreased drastically with relatively little change in the overall porosity. The sample deformed at an effective pressure of 40 MPa has a transitional mode of failure. It showed strain softening (Figure 2) and developed conjugate shear bands in the postfailure stage, but the nonhydrostatic loading caused significant reductions in permeability and porosity (Figure 3a) with a positive correlation between the two (Figure 4b).

Compared to porosity change, permeability is more variable from sample to sample. Some of the trends for permeability evolution in the brittle regime would be better defined if we plotted the data normalized to the initial values. However, we prefer to show here the primary data without normalization so that the reader can assess the data quality and sample variability. The porosity and permeability evolutions in the other sandstones (Figure 7) are qualitatively similar, with minor differences in the Darley Dale sandstone. As shown in Figure 7h, the Darley Dale

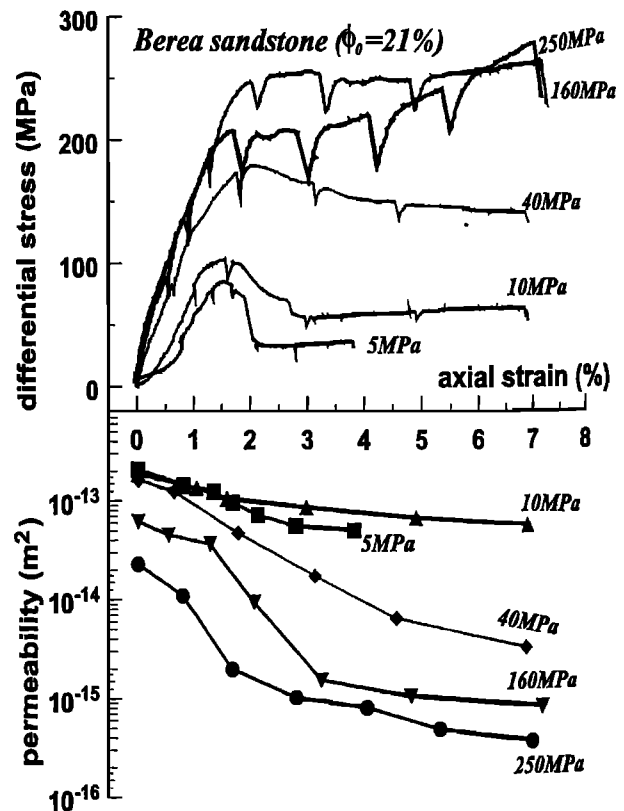


Figure 2. Experimental data for Berea sandstone. The differential stress and permeability are plotted versus axial strain. The effective pressures are as indicated.

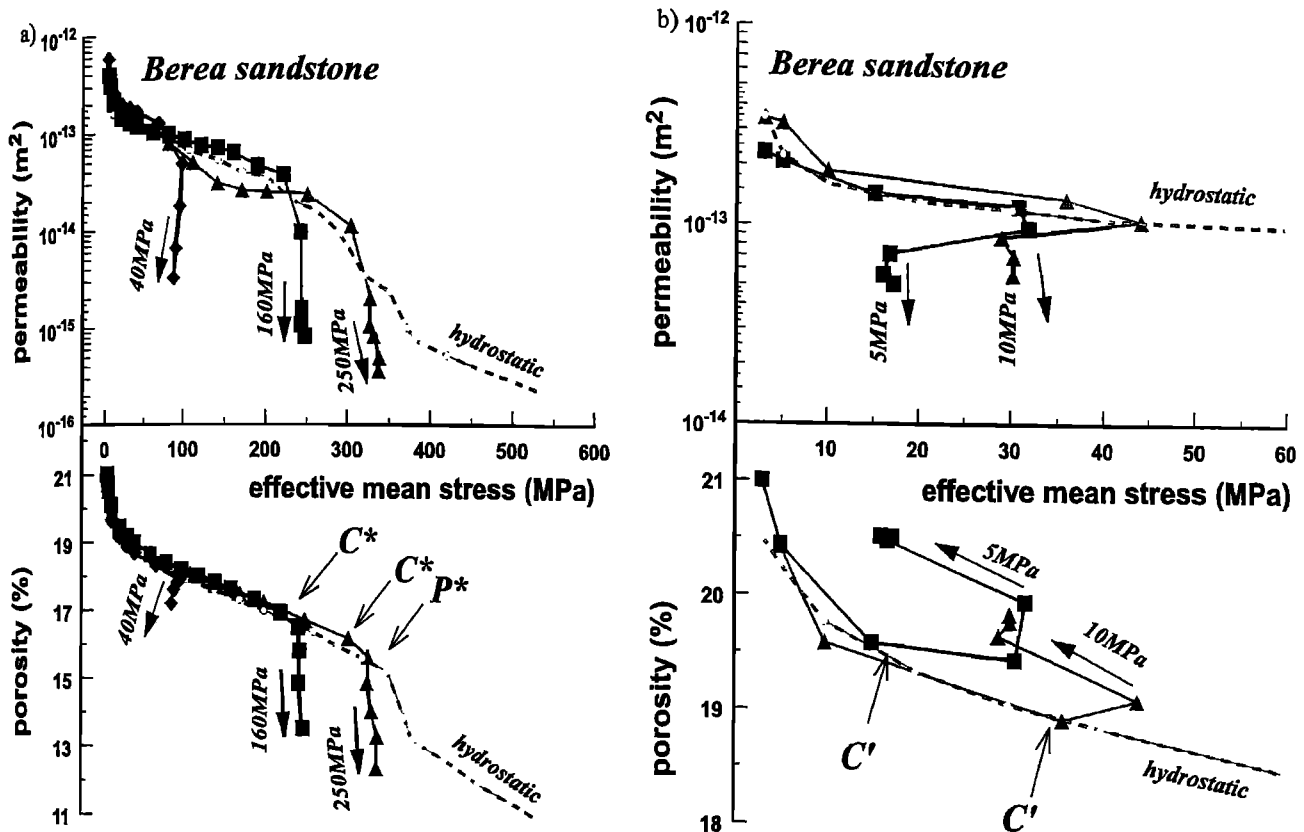


Figure 3. Permeability and porosity as functions of effective mean stress in the (a) cataclastic flow regime and (b) brittle faulting regime in Berea sandstone. For reference the data for the hydrostatic tests are shown as dashed curves. The effective pressures are as marked and the critical stress states  $C^*$ ,  $C'^*$ , and  $P^*$  are indicated by the open arrows.

sandstone samples (deformed at effective pressures of 5 and 10 MPa) did show a slight positive correlation between porosity and permeability but only in the region near the peak stresses. The Boise sandstone samples did not show any overall stress-induced dilation (Figure 7e). We suspect that dilation would occur if we were able to conduct experiments at lower effective pressures (which is not feasible since fluid leakage through the sample-jacket interface may occur).

## Discussion

### Shear-Enhanced Compaction: An Effective Mechanism for Permeability Reduction

A key conclusion we draw is that there is a one-to-one correspondence between porosity and permeability changes when a porous rock is deformed in the cataclastic flow regime. The compactive yield stress  $C^*$  maps out a boundary in the stress

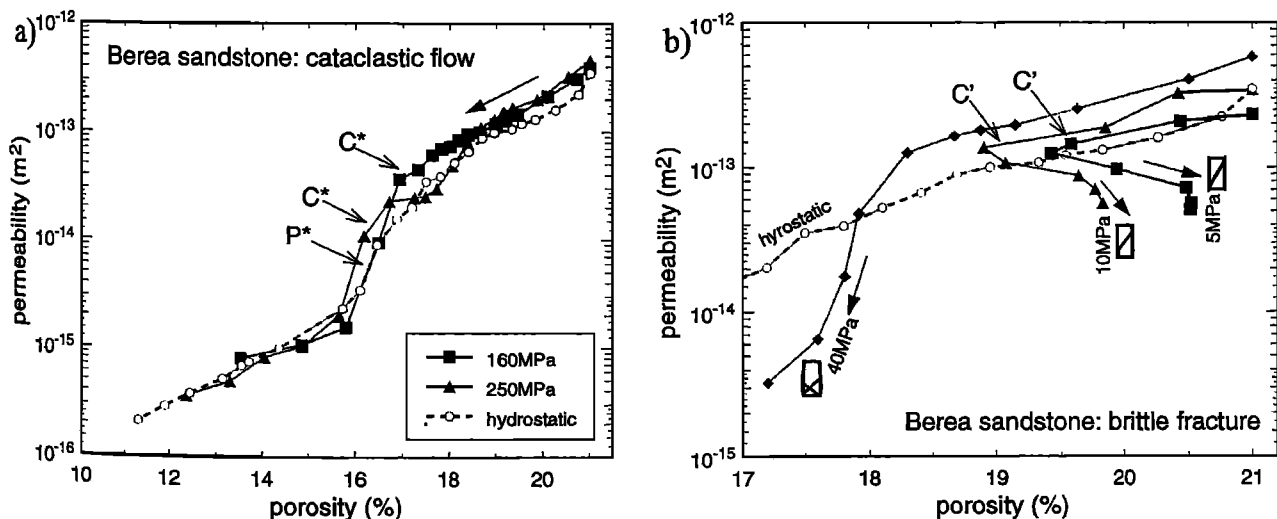


Figure 4. Permeability evolution as a function of porosity in Berea sandstone during (a) cataclastic flow and (b) brittle faulting. For reference the data for the hydrostatic tests are shown as dashed curves. The effective pressures are as marked, and the critical stress states  $C^*$  and  $C'$  are indicated by the open arrows.

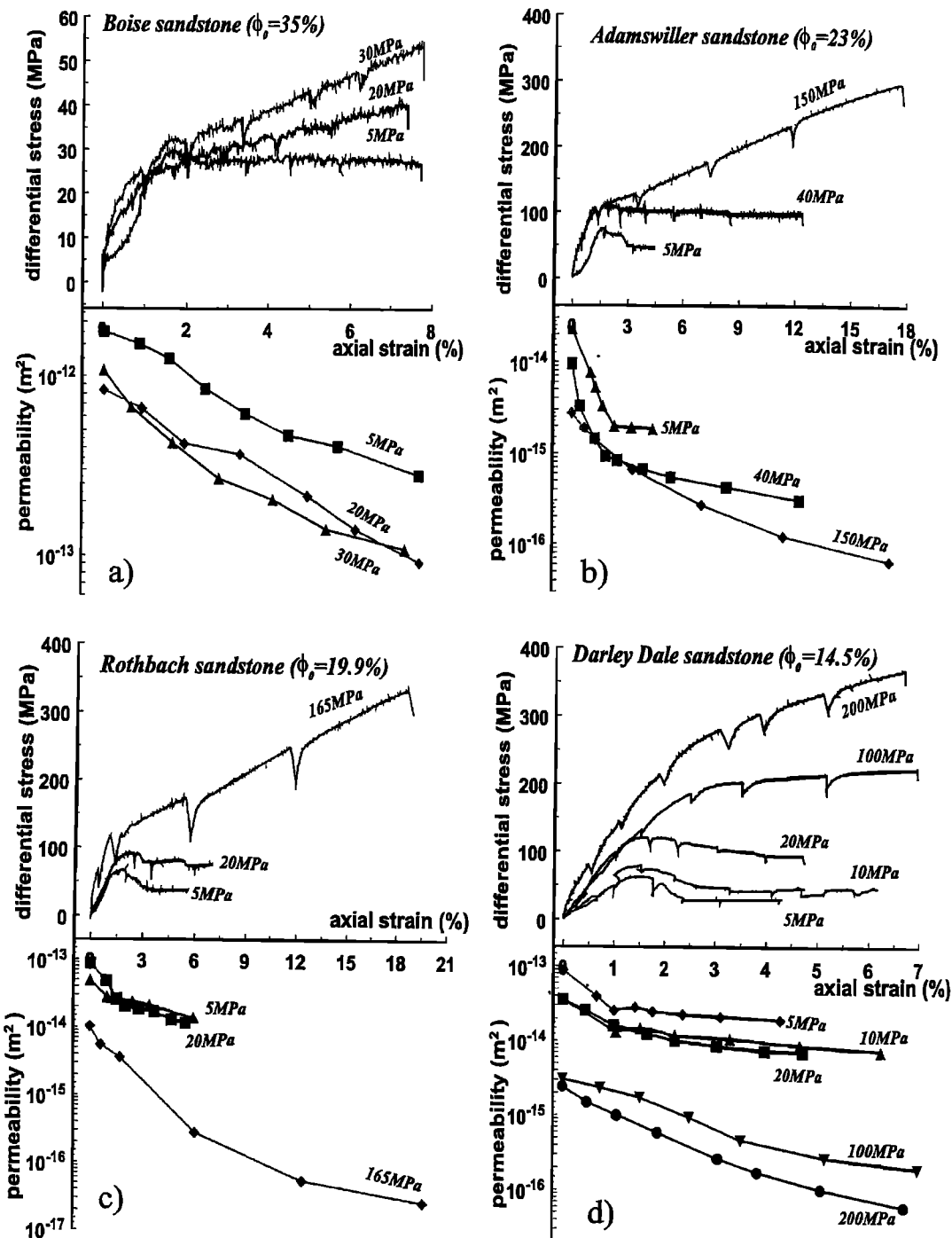


Figure 5. Experimental data for (a) Boise, (b) Adamswiller, (c) Rothbach, and (d) Darley Dale sandstones. The differential stress and permeability are plotted versus axial strain. The effective pressures are as indicated.

space separating two different types of permeability evolution. Before the critical stress  $C^*$  is attained, permeability and porosity both decrease with increasing hydrostatic loading, but their evolutions are independent of the deviatoric stress field. In other words, the deformation due to the deviatoric stresses is essentially elastic, with no influence on the porosity or permeability. The mechanisms for this type of behavior were discussed in some detail by David *et al.* [1994].

On the other hand, if the rock is stressed beyond  $C^*$ , the deviatoric stresses will cause significant inelastic compaction by

grain crushing and pore collapse [Wong *et al.*, this issue]. Consequently, both permeability and porosity changes are sensitively dependent on the deviatoric and hydrostatic loadings outside the  $C^*$  boundary (Figures 3a and 6). The damage associated with shear-enhanced compaction in Berea sandstone was characterized quantitatively by Menéndez *et al.* [1996]. Drastic decrease in pore size and increase in microcrack density were measured in samples deformed beyond  $C^*$ . These two factors would lower the local hydraulic conductances in individual pore channels and increase the "tortuosity" of the pore



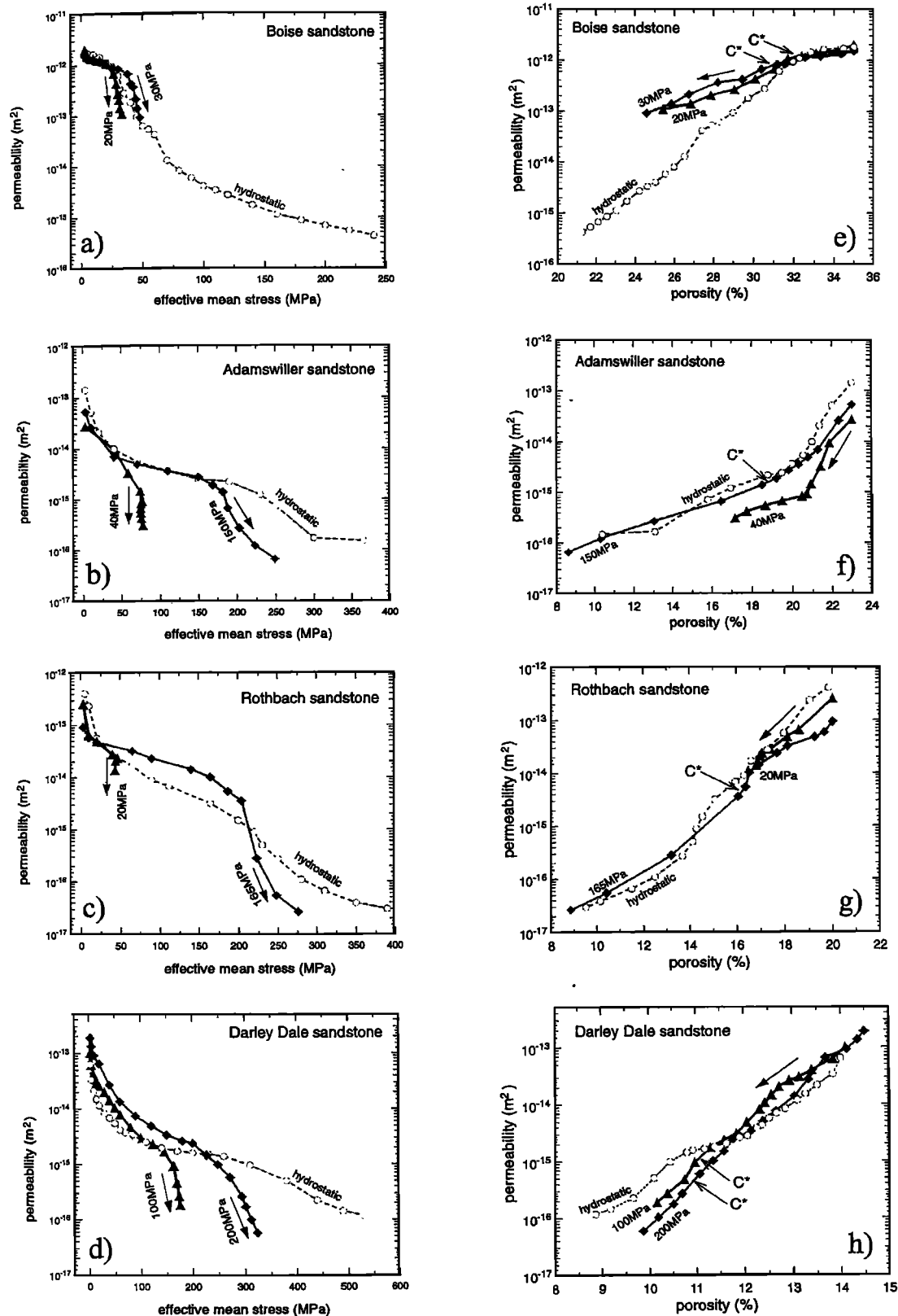


**Figure 6.** Permeability evolution during cataclastic flow. Permeability is plotted versus effective mean stress for (a) Boise, (b) Adamswiller, (c) Rothbach, and (d) Darley Dale sandstones. Permeability as a function of porosity is also plotted for (e) Boise, (f) Adamswiller, (g) Rothbach, and (h) Darley Dale sandstones. For reference the data for the hydrostatic tests are shown as dashed curves. The effective pressures are as marked, and the critical stress state  $C^*$  is indicated by the open arrows.

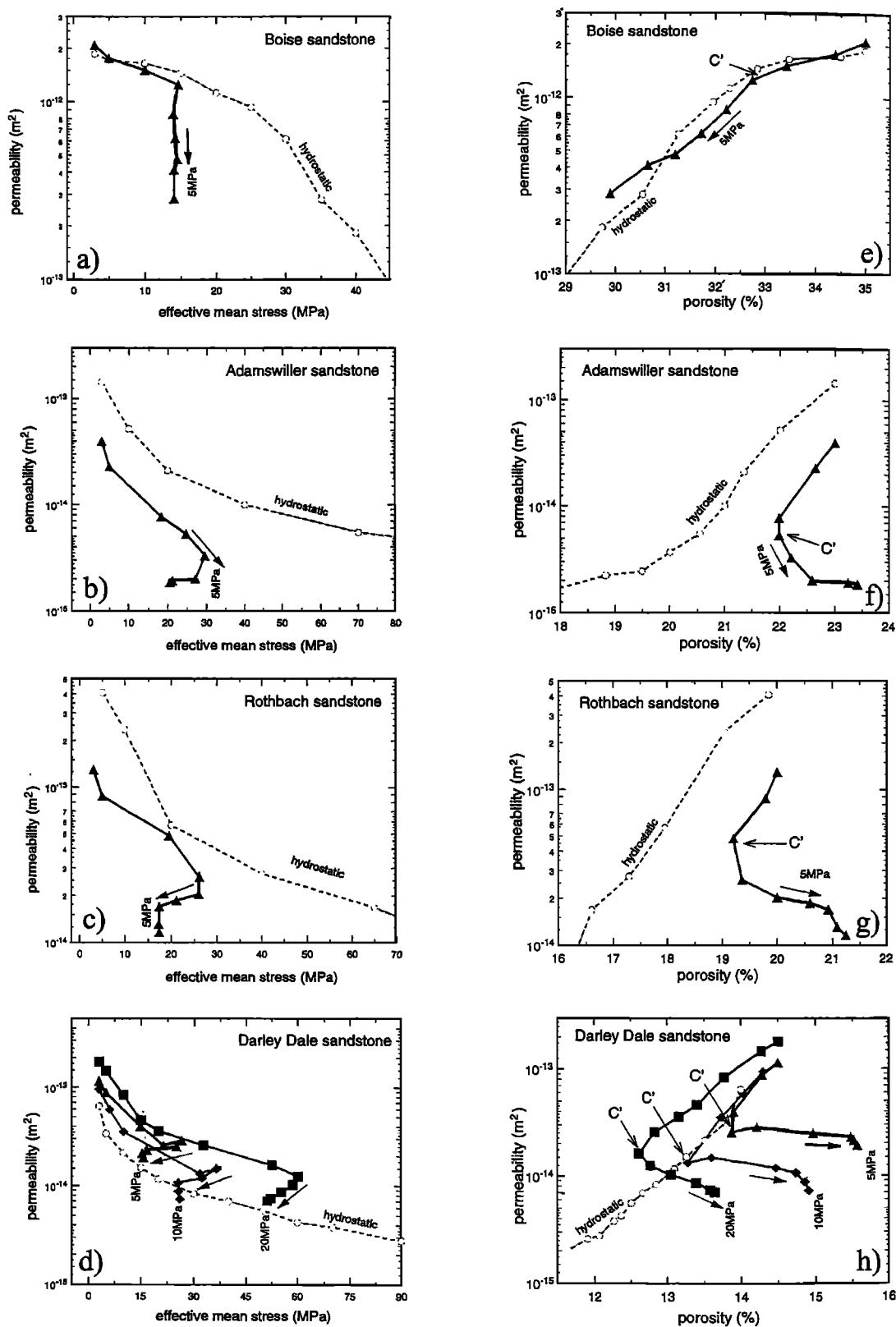


**Figure 7.** Permeability evolution during brittle faulting. Permeability is plotted versus effective mean stress for (a) Boise, (b) Adamswiller, (c) Rothbach, and (d) Darley Dale sandstones. Permeability as a function of porosity is also plotted for (e) Boise, (f) Adamswiller, (g) Rothbach, and (h) Darley Dale sandstones. For reference the data for the hydrostatic tests are shown as dashed curves. The effective pressures are as marked, and the critical stress state  $C^*$  is indicated by the open arrows.

space, resulting in an overall decrease in the permeability. The quantitative modeling of the permeability reduction mechanism is beyond the scope of the present study. Nevertheless, this is an important problem that needs to be investigated in the future.

The laboratory data show that the compactive yield stresses decrease with increasing porosity and grain size, in accordance to a power law with an exponent of  $\sim -3/2$  [Wong *et al.*, this issue]. The observation that permeability decreases by several orders of magnitude at the initiation of shear-enhanced compaction implies that deformation and fluid transport may be coupled in a complex manner. Additional complications also arise because the hydromechanical properties are sensitive to the loading path [Rhett and Teufel, 1992] and they may obey effective stress laws that are variable with stress [Warpinski and Teufel, 1990].

#### Cataclastic Flow: Compactive Versus Dilatant

Cataclastic flow is characterized by homogeneously distributed microcracking without the development of shear localization in the rock. Recent experimental data on quartzofeldspathic rocks [Tullis and Yund, 1992; Hirth and Tullis, 1994], marble [Fredrich *et al.*, 1989], hot-pressed calcite [Zhang *et al.*, 1994], and salt [Peach and Spiers, 1996] have demonstrated that it is the key intermediate step in the transition from brittle faulting to fully plastic flow in low-porosity crystalline rocks. While cataclastic flow in low- and high-porosity rocks have common attributes, there exist important differences in the porosity change and deformation mechanisms. First, inelastic deformation in the former is associated with porosity increase, whereas that in the latter is associated with compaction. Second, shear localization in the former is inhibited because the stress-induced cracks are arrested by twinning and dislocation activity, whereas that in the latter is inhibited by grain crushing and pore collapse. How does the permeability evolution reflect these differences in deformation mechanisms?

The room temperature data for the dilatant yield stress  $C'$  for calcite [Fredrich *et al.*, 1989; Zhang *et al.*, 1994] suggested that the differential stress  $C'$  for the onset of dilatant cataclastic flow increases with increasing effective mean stress. This is in contrast to the yield stress  $C^*$  for compactive cataclastic flow which decreases with increasing effective mean stress [Wong *et al.*, this issue]. Since the onset of dilatant cataclastic flow involves the interplay of microcracking and crystal plasticity processes, the magnitude of the critical stress  $C'$  is dependent on the yield stress for the onset of twinning and dislocation activity. For a given lithology,  $C'$  is also controlled by the grain size [Fredrich *et al.*, 1990].

Zhang *et al.* [1994] recently investigated the permeability evolution in Carrara marble and hot-pressed calcite. Peach and Spiers [1996] studied a natural rock salt (Asse Speisesalz), a synthetic fine-grained salt and salt/anhydrite rock, and Stormont and Daemen [1992] studied the Waste Isolation Pilot Plant (WIPP) rock salt. Before the critical stress  $C'$  is attained, the permeability change is dominated by the hydrostatic compaction due to elastic crack closure [Brace *et al.*, 1968], with little dependence on the deviatoric stresses. However, significant permeability increase is induced by the stress with the onset of dilatancy at  $C'$ . Two typical data sets of permeability data as a function of porosity are shown in Figure 8a. The initiation of dilatancy is associated with pervasive stress-induced microcracking [Fredrich *et al.*, 1989; Zhang *et al.*, 1994], which in turn causes permeability to increase rapidly as a function of porosity. Appealing to Gueguen and Dienes' [1989] percolation model for a cracked solid, Peach and Spiers [1996] concluded that his permeability data can be explained by a monotonic

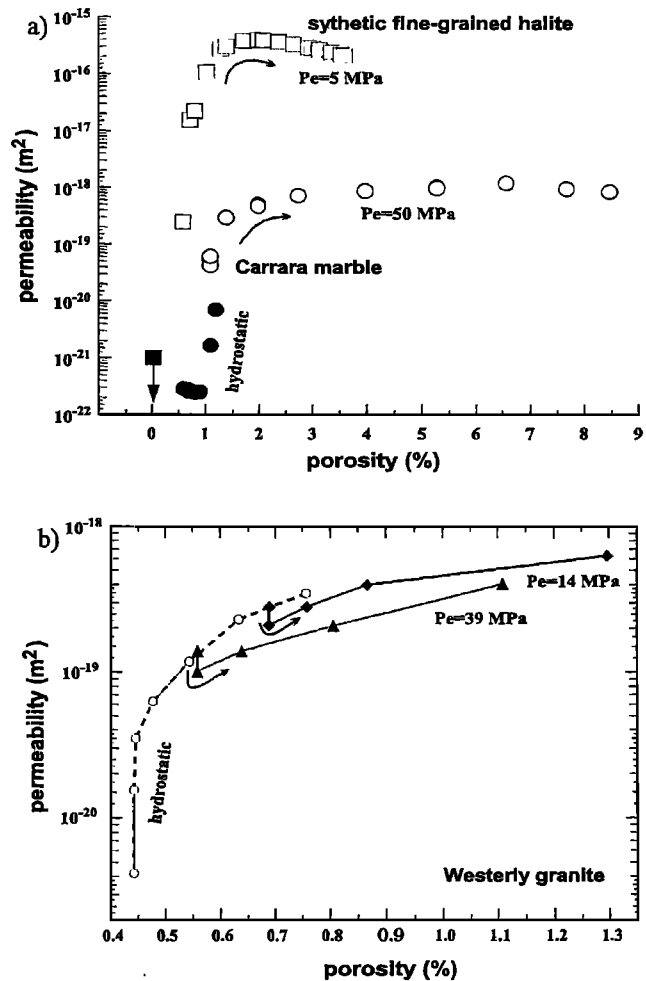


**Figure 8.** (a) Permeability evolution as a function of porosity during dilatant cataclastic flow in low-porosity rocks. The open squares are salt data by Peach and Spiers [1996], and the open circles are marble data by Zhang *et al.* [1994]. For reference the hydrostatic data for Carrara marble by Fischer and Paterson [1992] are shown as solid circles. The solid square indicates that the initial permeability was too low to be resolved by Peach and Spiers [1996]. (b) Permeability evolution during brittle faulting for Westerly granite [Zoback and Byerlee, 1975]. Permeability is plotted versus porosity. The effective pressures are as indicated. For reference the data for the hydrostatic tests [Brace *et al.*, 1968] are shown as the dashed curve.

increase in connectivity in the vicinity of  $C'$ . This is in contrast to the role of pervasive stress-induced cracking at the onset of shear-enhanced compaction which, as we discussed above, causes the connectivity to decrease in a porous rock. It is interesting to note from Figure 8a that as the porosity increases with the development of cataclastic flow, permeability actually decreases slightly with increasing porosity, implying that at this stage the role of microcracking has been reversed and the "tortuosity" of the pore space actually increases with damage accumulation.

Fully plastic flow with negligible porosity change was observed in Carrara marble [Fredrich *et al.*, 1989] and synthetic fine-grained salt [Peach and Spiers, 1996] at effective pressures of 300 and 20 MPa, respectively. How does permeability evolve in the transition from dilatant cataclastic flow to fully plastic flow? Peach and Spiers [1996] was not able to resolve the

permeability in the fully plastic salt sample because it was too low ( $k < 10^{-21}$  m<sup>2</sup>). *Brace* [1980] suggested that the development of fully plastic flow can eliminate all the interconnected porosity, ultimately leading to the percolation threshold [*Stauffer and Aharony*, 1992]. The scenario is probably analogous to the permeability evolution during cementation and hot-pressing, which in the final stage involves significant decrease in the connectivity of the pore space [*Zhu et al.*, 1995]. There are additional complications that are not fully understood. If the plastic flow causes the porosity reduction to exceed a certain critical rate, nearly lithostatic pore pressure may develop and hydraulic fracturing may occur [*Walder and Nur*, 1984]. In quartzo-feldspathic rocks, the brittle-plastic transition requires both elevated pressures and temperatures [*Tullis and Yund*, 1992; *Hirth and Tullis*, 1994]. The influence of temperature and strain rate on permeability evolution needs to be investigated.

We have emphasized here the fundamental differences between compactive and dilatant cataclastic flow in high- and low-porosity rocks. However, we have not addressed the question: at what porosity will the transition from dilatant to compactive cataclastic flow occur? A value of ~5% was suggested by *Brace* [1978b] without elaborating on how he arrived at this particular choice. From the previous discussion of the deformation mechanisms, one would speculate that the transition occurs in a rock of intermediate porosity with the interplay of microcracking, pore collapse, twinning, and possibly dislocation activity. To our knowledge, the most relevant data on this transition are from room temperature experiments on Solnhofen limestone [*Edmond and Paterson*, 1972; *Fischer and*

*Paterson*, 1989; *Fredrich et al.*, 1990]. Collectively, these three studies show that dilatant cataclastic flow occurs at effective pressures ranging from 70 to 250 MPa, and compactive cataclastic flow occurs at 300-800 MPa. The transition from dilatant to compactive cataclastic flow therefore occurs at an effective pressure of ~250 MPa. According to *Fischer and Paterson's* [1989] data, the porosity of Solnhofen limestone at 250 MPa pressure is 5.6%, in good agreement with *Brace's* [1978b] suggestion.

#### Evolution of Permeability: Brittle Faulting

Our key observation on the evolution of permeability in the brittle fracture regime is that although the sample dilates prior to failure, permeability will actually decrease in a porous sandstone. This is in contrast to observations in low-porosity rocks that permeability generally increases prior to brittle fracture. To make comparison with these data, we have replotted the permeability data of Westerly granite for hydrostatic [*Brace et al.*, 1968] and triaxial [*Zoback and Byerlee*, 1975] compression in Figure 8b. The latter study was conducted on samples stressed to ~80% of the peak stress. Comparison with our data (Figures 4b and 7) indicates that the behavior in Westerly granite and Darley Dale sandstone are similar in that both show positive correlations of porosity and permeability change from  $C'$  to the peak stress. In contrast, the other four sandstones all show negative correlations.

To characterize the permeability evolution in the brittle regime, we introduce the parameter  $\xi = [k(\text{peak stress}) - k(C')]/k(C')$  which corresponds to the change in permeability

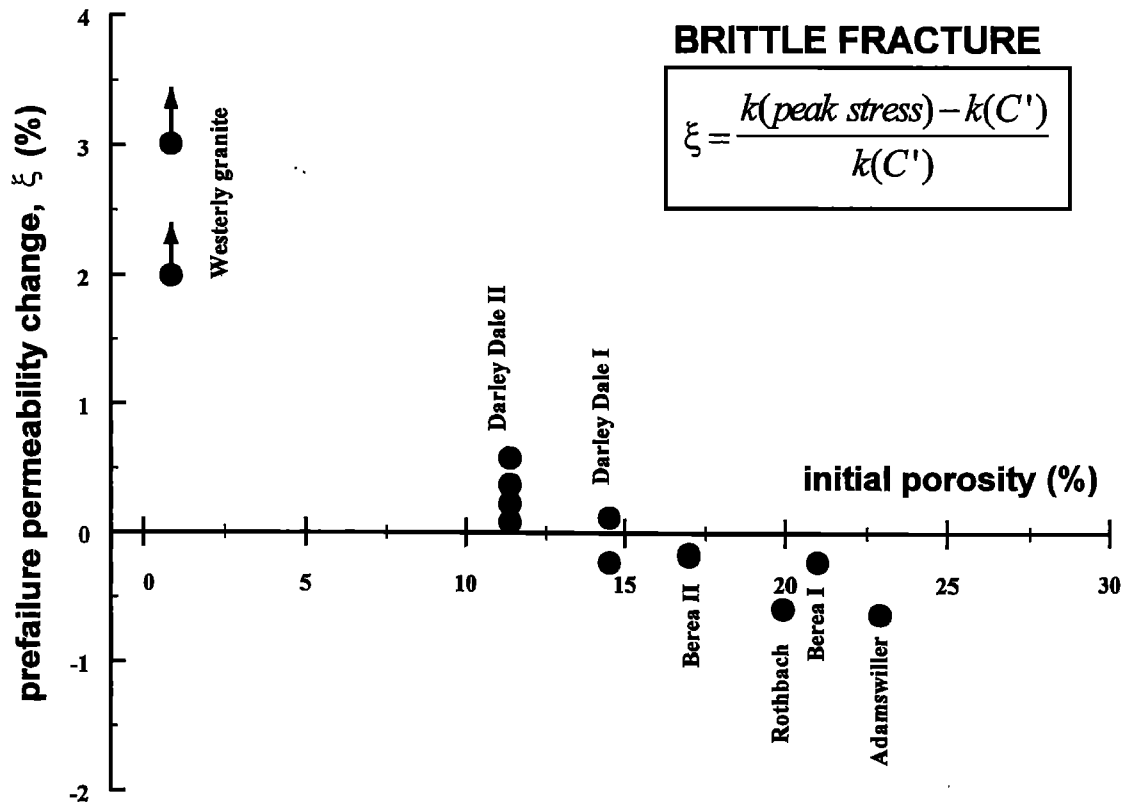


Figure 9. Prefailure permeability change as a function of initial porosity in the brittle regime. Data of Darley Dale II are from *Mordecai and Morris* [1971]. Data of Berea II are from *Gatto* [1984]. Data of Westerly granite were reported by *Zoback and Byerlee* [1975] for samples loaded to ~80% of the peak stress. The arrows indicate that these values are lower bounds. Multiple values for Westerly granite, Darley Dale I and II sandstones, and Berea I and II sandstones are for triaxial compression tests at different effective pressures.

when a sample is loaded from  $C'$  to the peak stress, normalized to the permeability value at  $C'$ . The parameter  $\xi$  as defined here is somewhat different from the percentage change calculated by *Brace* [1978a], who used the permeability under hydrostatic loading as the reference. Figure 9 shows the prefailure permeability change  $\xi$  as a function of initial porosity. Other than our data (for all samples which showed overall dilation prior to brittle failure), we have included *Zoback and Byerlee's* [1975] data for Westerly granite, *Mordecai and Morris'* [1971] data for an 11% porosity Darley Dale sandstone, and *Gatto's* [1984] data for a 17% porosity Berea sandstone. The data define a trend for the prefailure permeability change  $\xi$  to decrease with increasing initial porosity.

It should be noted that our permeability values for Darley Dale sandstone are lower than *Mordecai and Morris'* [1971] gas permeability values at comparable effective pressures by about half an order of magnitude. This is not surprising since the latter samples had lower porosities. However, the same explanation can not be applied to our data for Berea sandstone which are comparable to *Gatto's* [1984] gas permeability values at comparable effective pressures, even though the porosities of the latter samples were lower by  $\sim 4\%$ . The discrepancy may be attributed to two factors: the difference in chemistry and hydrodynamics of water and gas, and sample variability.

The experimental data show that permeability decreases monotonically with deformation for sandstones with porosities greater than 15%, and even in a low-porosity sandstone (such as the Darley Dale) the prefailure permeability change is relatively small. This intriguing phenomenon of permeability reduction in a dilating sandstone can only be explained by a dramatic increase in the "tortuosity" of the pore space due to microcracking. To better visualize the "tortuosity" change and to gain deeper insight into the complex interplay of cracks and tubular pores, we developed a network model [*Zhu and Wong, 1996*] on the basis of microstructural data of *Menéndez et al.* [1996]. The experimental data also show that permeability decreases with increasing deformation in the postpeak stage. After a throughgoing shear band has developed, the permeability evolution is expected to be similar to *Teufel's* [1987] observations for fractured Coconino sandstone (of initial porosity 10%) with permeability decreasing with increasing shear displacement in the gouge zone. Although we only consider consolidated rocks in Figure 9, other experimental data on unconsolidated materials, including Ottawa sand [*Zoback and Byerlee, 1976*] and quartz/clay mixture [*Brown et al., 1994*], also show negative values of  $\xi$  comparable to those for the more porous sandstones investigated here. Permeability may decrease further in the presence of healing and sealing processes under hydrothermal conditions [*Zhu et al., 1995*].

Therefore it is unlikely that tectonic faulting in porous rock formations and shear displacement along gouge zones can provide conduits for massive flux of fluid along seismogenic zones. Field observations in sandstone formations [*Antonellini and Aydin, 1994*] seem to support this conclusion. However, it should be noted that the interpretation here assumes constant hydrostatic loading. The laboratory data show that a decrease in effective mean stress (which may occur by a decrease in the mean stress or an increase in pore pressure) can be very effective in enhancing the permeability. A decrease in mean stress may result from a process such as the coseismic stress drop. Significant pore pressure excess may result from numerous mechanisms that have been identified in igneous, metamorphic, and sedimentary settings [*Bredehoeft and Hanshaw, 1968*]. The tectonic deformation, healing, and sealing processes may act

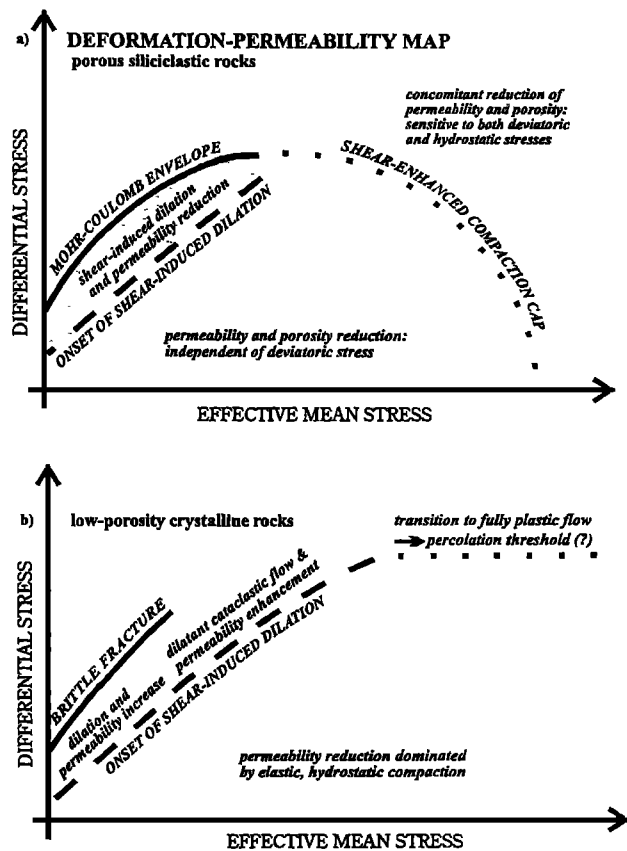


Figure 10. Deformation-permeability map for (a) porous siliciclastic rocks and (b) low-porosity crystalline rocks.

together to reduce the permeability to a low level, thus providing a favorable hydromechanical environment for the maintenance of such pore pressure excesses. If the pore pressure builds up to nearly lithostatic, then hydrofracturing may provide conduits for focused fluid transport within fault zones, in a scenario similar to that proposed by *Brown et al.* [1994] for accretionary wedges.

### Deformation-Permeability Maps

Our study has focused on the relations among stress, porosity, and permeability. Permeability was only measured in the axial ( $\sigma_1$ ) direction. Recent data on stressed sandstones [*Bruno, 1994; Zhu et al., 1996*] have shown that significant permeability anisotropy is associated with both brittle faulting and cataclastic flow. Our data on permeability in the  $\sigma_1$  direction represent maximum tensor values. On the basis of permeability data presented here and mechanical deformation data of *Wong et al.* [this issue], we propose a deformation-permeability map (Figure 10a) as a conceptual model for the coupling of deformation and fluid transport in porous siliciclastic rocks. The critical stresses for the onset of shear-induced dilation ( $C'$ ) and of shear-enhanced compaction ( $C^*$ ) map out the boundary of a closed domain in the stress space, within which porosity and permeability decrease with increasing hydrostatic loading, with negligible dependence on the deviatoric stresses. In the cataclastic flow regime, the compactive yield stresses  $C^*$  map out an elliptical cap in the stress space [*Wong et al., this issue, Figure 8*], which expands with decreasing porosity and grain size. If the rock is loaded to beyond this cap, significant permeability

reduction results from the development of shear-enhanced compaction and cataclastic flow (Figures 3a and 6). In the brittle regime, if the rock is stressed to beyond  $C'$  under relatively low effective pressures, then a complex interplay of shear-induced dilation and permeability decrease may occur (Figures 3b and 7). After the peak stress (mapped out by the Mohr-Coulomb fracture envelope) has been attained, the rock usually shows accelerating permeability reduction with the development of shear localization.

Comparison of our data with mechanical deformation and permeability data on low-porosity calcite and halite aggregates show fundamental differences. To illustrate these differences, we also summarize these data by a schematic deformation-permeability map (Figure 10b). In a low-porosity crystalline rock (with porosity less than 5% or so), significant dilatancy is observed in both the brittle faulting and cataclastic flow regime. However, no porosity change occurs after the deformation mechanism has undergone the transition to fully plastic flow. Therefore the critical stresses for the onset of dilatancy  $C'$  and for plastic flow map out the boundary below which permeability decreases because of the elastic, hydrostatic compaction of a rock permeated by preexisting microcracks. As soon as the rock is loaded to beyond the  $C'$  boundary significant permeability enhancement is expected in both the brittle faulting and cataclastic flow regimes. However, under elevated effective pressures (and also elevated temperatures for quartz-feldspathic rocks), a transition from dilatant cataclastic flow to fully plastic flow occurs if the differential stress exceeds the yield stress, and the permeability is expected to decrease. The development of plastic flow may eliminate the interconnected porosity and ultimately lead to an impermeable rock, corresponding to the percolation threshold.

**Acknowledgments.** Pilot experiments on the Adamswiller and Rothbach sandstones were initiated by Christian David. We thank John Logan for drawing our attention to the Berea sandstone data in Henrietta Gatto's thesis. We have benefited from discussions with Yves Bernabé, Christian David, Joanne Fredrich, John Logan, Beatriz Menéndez, and Bernard Seront. We also thank Mike Batzle, Steve Mackwell, and Larry Myer for their critical reviews. This research was supported by the National Science Foundation under grants EAR9219589 and EAR9508044.

## References

- Antonellini, M., and A. Aydin, Effect of faulting on fluid flow in porous sandstones: Petrophysical properties, *AAPG Bull.*, 78, 355-377, 1994.
- Bernabé, Y., A wide range permeameter for use in rock physics, *Int. J. Rock Mech. Min. Sci.*, 24, 309-315, 1987.
- Brace, W.F., A note on permeability change in geologic materials due to stress, *Pure Appl. Geophys.*, 116, 627-633, 1978a.
- Brace, W.F., Volume changes during fracture and frictional sliding: A review, *Pure Appl. Geophys.*, 116, 603-614, 1978b.
- Brace, W.F., Permeability of crystalline and argillaceous rocks, *Int. J. Rock Mech. Min. Sci.*, 17, 241-251, 1980.
- Brace, W.F., J.B. Walsh, and W.T. Frangos, Permeability of granite under high pressure, *J. Geophys. Res.*, 73, 2225-2236, 1968.
- Bredehoeft, J.D., and B.B. Hanshaw, On the maintenance of anomalous fluid pressures, I, Thick sedimentary sequences, *Geol. Soc. Am. Bull.*, 79, 1097-1106, 1968.
- Bredehoeft, J.D., and D.L. Norton (Eds.), *The Role of Fluid in Crustal Processes*, 170 pp., Nat. Acad. Press, Washington, D. C., 1990.
- Brown, K.M., B. Bekins, B. Clennell, D. Dewhurst, and G. Westbrook, Heterogeneous hydrofracture development and accretionary fault dynamics, *Geology*, 22, 259-262, 1994.
- Bruno, M.S., Micromechanics of stress-induced permeability anisotropy and damage in sedimentary rock, *Mech. Mater.*, 18, 31-48, 1994.
- David, C., T.-f. Wong, W. Zhu, and J. Zhang, Laboratory measurement of compaction-induced permeability change in porous rock: Implications for the generation and maintenance of pore pressure excess in the crust, *Pure Appl. Geophys.*, 143, 425-456, 1994.
- Edmond, J.M., and M.S. Paterson, Volume change during the deformation of rocks at high pressure, *Int. J. Rock Mech. Min. Sci.*, 9, 161-182, 1972.
- Fischer, G.J., and M.S. Paterson, Dilatancy during rock deformation at high temperatures and pressures, *J. Geophys. Res.*, 94, 17607-17618, 1989.
- Fischer, G.J., and M.S. Paterson, Measurement of permeability and storage capacity in rocks during deformation at high temperature and pressure, in *Fault Mechanics and Transport Properties of Rocks*, edited by B. Evans and T.-f. Wong, pp. 213-252, Academic Press, San Diego, 1992.
- Fredrich, J.T., B. Evans, and T.-f. Wong, Micromechanics of the brittle to plastic transition in Carrara marble, *J. Geophys. Res.*, 94, 4129-4145, 1989.
- Fredrich, J., B. Evans, and T.-f. Wong, Effects of grain size on brittle and semibrittle strength: Implications for micromechanical modeling of failure in compression, *J. Geophys. Res.*, 95, 10907-10920, 1990.
- Gatto, H.G., The effect of various states of stress the permeability of Berea sandstone, M.S. thesis, Texas A&M Univ., College Station, 1984.
- Gueguen, Y., and J. Dienes, Transport properties of rocks from statistics and percolation, *Math. Geol.*, 21, 1-13, 1989.
- Hirth, G., and J. Tullis, The brittle-plastic transition in experimentally deformed quartz aggregates, *J. Geophys. Res.*, 99, 11731-11748, 1994.
- Holt, R.M., Permeability reduction induced by a non-hydrostatic stress field, paper SPE19595 presented at 64th Annual Technical Conference, Soc. of Pet. Eng., San Antonio, TX, 1989.
- Hsieh, P.A., J.V. Tracy, C.E. Neuzil, J.D. Bredehoeft, and S.E.A. Silliman, A transient laboratory method for determining the hydraulic properties of "tight" rocks, I, Theory, *Int. J. Rock Mech. Min. Sci. Geomech. Abstr.*, 18, 245-252, 1981.
- Menéndez, B., W. Zhu, and T.-f. Wong, Micromechanics of brittle faulting and cataclastic flow in Berea sandstone, *J. Struct. Geol.*, 18, 1-16, 1996.
- Mordecai, M., and L.H. Morris, An investigation into the changes of permeability occurring in a sandstone when failed under triaxial stress conditions, *Proc. U.S. Rock Mech. Symp.*, 12, 221-239, 1971.
- Nelson, R.A., A discussion of the approximation of subsurface (burial) stress conditions in laboratory experiments, in *Mechanical Behavior of Crustal Rocks, The Handin Volume*, Geophys. Monogr. Ser., Vol. 24, edited by N.L. Carter, M. Friedman, J.M. Logan, and D.W. Stearns, pp. 311-322, AGU, Washington, D. C., 1981.
- Neuzil, C.E., C. Cooley, S.E. Silliman, J.D. Bredehoeft, and P.A. Hsieh, A transient laboratory method for determining the hydraulic properties of "tight" rocks, 2, Application, *Int. J. Rock Mech. Min. Sci.*, 18, 253-258, 1981.
- Peach, C.J., and C.J. Spiers, Influence of crystal plastic deformation on dilatancy and permeability development in synthetic salt rock, *Tectonophysics*, 256, 101-128, 1996.
- Rhett, D.W., and L.W. Teufel, Stress path dependence of matrix permeability of North Sea sandstone reservoir rock, *Proc. U.S. Rock Mech. Symp.*, 33, 345-354, 1992.
- Somerton, W.H., I.M. Soylemezoglu, and R.C. Dudley, Effect of stress on permeability of coal, *Int. J. Rock Mech. Min. Sci.*, 12, 129-145, 1975.
- Stauffer, D., and A. Aharony, *Introduction to Percolation Theory*, 181 pp., Taylor and Francis, Bristol, Pa., 1992.
- Stormont, J.C., and J.J.K. Daemen, Laboratory study of gas permeability changes in rock salt during deformation, *Int. J. Rock Mech. Min. Sci.*, 29, 323-342, 1992.
- Teufel, L.W., Permeability changes during shearing deformation of fractured rock, *Proc. U.S. Rock Mech. Symp.*, 28, 473-480, 1987.
- Torgersen, T., Crustal-scale fluid transport: Magnitude and mechanisms, *Geophys. Res. Lett.*, 18, 917-918, 1991.
- Tullis, J., and R.A. Yund, The brittle-ductile transition in feldspar aggregates: An experimental study, in *Fault Mechanics and*

- Transport Properties of Rocks*, edited by B. Evans and T.-f. Wong, pp. 89-117, Academic, San Diego, Calif., 1992.
- Walder, J., and A. Nur, Porosity reduction and crustal pore pressure development, *J. Geophys. Res.*, **89**, 11539-11548, 1984.
- Warpinski, N.R., and L.W. Teufel, Determination of the effective stress law for permeability and deformation in low-permeability rocks, paper SPE20572 presented at 65<sup>th</sup> Annual Technical Conference, Soc. of Pet. Eng., New Orleans, LA, 1990.
- Wong, T.-f., C. David, and W. Zhu, The transition from brittle faulting to cataclastic flow in porous sandstones: Mechanical deformation, *J. Geophys. Res.*, this issue.
- Zhang, S., S.F. Cox, and M.S. Paterson, The influence of room temperature deformation on porosity and permeability in calcite aggregates, *J. Geophys. Res.*, **99**, 15761-15775, 1994.
- Zhu, W., C. David, and T.-f. Wong, Network modeling of permeability evolution during cementation and hot isostatic pressing, *J. Geophys. Res.*, **100**, 15451-15464, 1995.
- Zhu, W., L. Montesi, and T.-f. Wong, Shear-enhanced compaction and permeability reduction: triaxial extension tests on porous sandstone, *Mech. Mater.*, in press, 1996.
- Zhu, W., and T.-f. Wong, Permeability reduction in a dilating rock: Network modeling of damage and tortuosity, *Geophys. Res. Lett.*, **23**, 3099-3102, 1996.
- Zoback, M.D., and J.D. Byerlee, The effect of microcrack dilatancy on the permeability of Westerly granite, *J. Geophys. Res.*, **80**, 752-755, 1975.
- Zoback, M.D., and J.D. Byerlee, Effect of high-pressure deformation on permeability of Ottawa Sand, *AAPG Bull.*, **60**, 1531-1542, 1976.

---

T.-f. Wong and W. Zhu, Department of Earth and Space Sciences, State University of New York, Stony Brook, NY 11794-2100, (e-mail: wong@seism1.ess.sunysb.edu; zhu@seism1.ess.sunysb.edu)

(Received March 1, 1996; revised October 14, 1996; accepted October 21, 1996.)